


Research Article

Investigations of Coal-Rock Parting-Coal Structure (CRCS) Slip and Instability by Excavation

Guang-Jian Liu,¹ Heng Zhang ,² Ya-Wei Zhu,² Wen-Hao Cao,² Xian-Jun Ji,² Cai-Ping Lu,³ and Yang Liu³

¹Key Laboratory of Rock Mechanics and Geohazards of Zhejiang Province, Shaoxing University, Shaoxing, Zhejiang 312099, China

²School of Civil Engineering, Nanyang Institute of Technology, Nanyang, Henan 473004, China

³Key Laboratory of Deep Coal Resource Mining (Ministry of Education), School of Mines, China University of Mining and Technology, Xuzhou, Jiangsu 221116, China

Correspondence should be addressed to Heng Zhang; hzhangcumt@126.com

Received 19 July 2021; Accepted 6 August 2021; Published 19 August 2021

Academic Editor: Antonio Giuffrida

Copyright © 2021 Guang-Jian Liu et al. This is an open access article distributed under the Creative Commons Attribution License, which permits unrestricted use, distribution, and reproduction in any medium, provided the original work is properly cited.

Slip and instability of coal-rock parting-coal structure (CRCS) subjected to excavation disturbance can easily induce coal-rock dynamic phenomena in deep coal mines. In this paper, the failure characteristics and influencing factors of CRCS slip and instability were investigated by theoretical analysis, numerical simulations, and field observations. The following main results are addressed: (1) the slip and instability of CRCS induced by excavation are due to stress release, and the damage of the rock parting is partitioned into three parts: shear failure zone, slipping zone, and splitting failure zone from inside to outside with slip; (2) the slip and instability process of CRCS is accompanied by initiation, expansion, and intersection of shear and tensile cracks. The development of the cracks is dominated by shear behaviour, while the tensile crack is the main factor affecting fracture and instability of CRCS; and (3) slip and instability of CRCS are characterized by stick-slip first and then stable slip, accompanied with high P-wave velocity and rockburst danger coefficient based on microseismic tomography.

1. Introduction

The diversity of sedimentary components and environments in different geological periods caused rock parting embedded in coal seams [1, 2]. The rock parting fabricates structural interfaces (discontinuities) between the coal and rock, which significantly changes the structure and mechanical properties of the coal. The potential slip and fracture of the discontinuities may trigger the dynamic instability of the coal-rock parting-coal structure (CRCS). On one hand, the slip and fracture along the weak discontinuities of coal-rock can be triggered due to excavation disturbances [3–7]. On the other hand, there exists asynchronism characteristics of crack development in CRCS due to strength differences between coal and rock parting, the

inharmonious development of cracks will cause the partitioned destruction of CRCS, and the local destruction and instability are thus induced [8].

At present, the deformation and failure characteristics of compound samples (coal-rock or rock-rock) have been fruitfully investigated in laboratory [9–13]. Some researchers found that the slip and instability of coal-rock combinations may be due to shear failure [14–19]. However, these studies mainly focused on the fracture of two-body structure, for example, “roof-coal” or three-body structure, for example, “roof-coal-floor,” without considering the influence of rock parting on slip and instability of CRCS. Field observations are also limited by geological and mining factors, which is difficult to directly reflect the process of crack development and slip of CRCS.

Recently, numerical simulation has a wide range of applications in the field of rock mechanics. The Universal Distinct Element Code (UDEC) is a two-dimensional discrete element program dealing with discontinuous media. It can be used to study the progressive failure of rock slope and evaluate the effects of joints, cracks, faults, and layers of rock mass on underground engineering and rock foundation. For example, Alzo'ubi reproduced typical rock slope failure (i.e. toppling and buckling) using the UDEC-GBM method [20, 21]. Gao et al. improved the Voronoi logic and got the UDEC-Trigon block model of more realistic to model fracture patterns and simulated the process of crack development around roadways [22, 23]. Zheng et al. studied the mechanisms of flexural toppling failure in anti-inclined rock slopes using UDEC-Trigon method [24]. Lu et al. investigated the slip-instability process of coal seam roadway with rock parting under dynamic loading using the UDEC-Trigon block model [25].

In summary, the UDEC-Trigon numerical simulation can intuitively reflect the process of crack development and slip of coal-rock structures, which makes up for the deficiency of field observation. In this paper, the micro-mechanical parameters of coal and rock parting were first calibrated by numerical simulations. Then, the coupling method of Trigon and rectangular blocks was used to investigate the effects of excavation and mining on slip and instability of CRCS. Finally, the results obtained from numerical simulations were verified by field observations in the 7301 working face of the Zhaolou coal mine (ZCM). The research results help us to understand the instability process of coal seam with rock parting, which is of great significance to prevent the occurrence of rockburst in advance.

2. Research Background

2.1. Introduction of the 7301 Working Face. The 7301 working face with buried depth of 962 to 1037 m is the first fully mechanized top-coal caving face in the #7 mining area of ZCM, with strike and slope lengths of 1678 and 230 m, respectively. The working face is characterized by strong rockburst danger. Its east is neighbour to the goaf of the 1303 working face, with the nearest distance of 55 m, the south is the designed 7303 working face, the west is the centralized tailentry of the #7 mining area, and the north is the boundaries of the #3 and #7 mining areas, as shown in Figure 1.

2.2. Geological Conditions. The mining seam is the 6.8 to 9.0 m thick 3# coal with 1° to 13° dip angle and average uniaxial compressive strength (UCS) of 16 MPa. A wedge-shaped rock parting layer at the east part of the 7301 working face bifurcated the 3# coal into 3_{upper#} and 3_{lower#} seams. Both thicknesses were 4.4 to 5.4 m with the average of 4.9 and 1.3–2.6 m with the average of 1.8 m, respectively. With extension inward into the cut and middle part of the 7301 working face, the thickness of the rock parting gradually reduced, as shown in Figure 1. Table 1 shows the physical

and mechanical properties of the rock parting, roof, and floor.

2.3. Mechanical Analysis of CRCS in the 7301 Working Face.

It is known that both driving and mining will cause the stress change and redistribution of surrounding coal and rock mass, but the effects of both actions on stress disturbance are different. The roadway excavation is a process of gradual stress release [26], while the mining is a progressive advancing of front abutment stress [27, 28]. If vertical stress acting on coal-rock interface increases (or the horizontal stress reduces), the original stress equilibrium state will be broken, resulting in failure mode change of coal-rock mass.

The mechanical model of CRCS (two interfaces between upper/or lower coal and medium rock parting have same stress condition) is shown in Figure 2. The maximum principal stress and the minimum principal stress are σ_1 and σ_3 , respectively, σ_{xy} is shear stress along the interface, and σ_{yy} is normal stress along the interface. The angle between the interface and the horizontal surface is δ . The friction angle of the interface is φ_f , and the cohesion is c . The normal stress and shear stress of the interface can be expressed as follows:

$$\sigma_{xy} = \frac{\sigma_1 - \sigma_3}{2} \sin 2\delta, \quad (1)$$

$$\sigma_{yy} = \frac{\sigma_1 + \sigma_3}{2} + \frac{\sigma_1 - \sigma_3}{2} \cos 2\delta. \quad (2)$$

According to the Coulomb-friction law, there exists a limit of shear strength for any interface.

$$\tau_f = \sigma_{yy} \cdot \tan \varphi_f + c. \quad (3)$$

Equation (2) is introduced into equation (3). When $\sigma_{xy} = \tau_f$, the criteria for determining the slip initiation of the interface are as follows:

$$(\sigma_1 - \sigma_3)_{\text{slip}} = \frac{2c}{(1 - \tan \varphi_f \cot \delta) \sin 2\delta} + \frac{2 \tan \varphi_f}{(1 - \tan \varphi_f \cot \delta) \sin 2\delta} \delta_3. \quad (4)$$

In equation (4), when $\delta = 90^\circ$ or $\delta \rightarrow \varphi_f$, $(\sigma_1 - \sigma_3) \rightarrow \infty$.

Then,

$$\varphi_f < \delta < 90^\circ, \quad (1 - \tan \varphi_f \cot \delta) \sin 2\delta > 0. \quad (5)$$

Therefore, σ_1 and σ_3 are monotonically increasing linear functions, as shown in Figure 3.

When the interface slips,

$$(\sigma_1 - \sigma_3) \geq (\sigma_1 - \sigma_3)_{\text{slip}}. \quad (6)$$

Then,

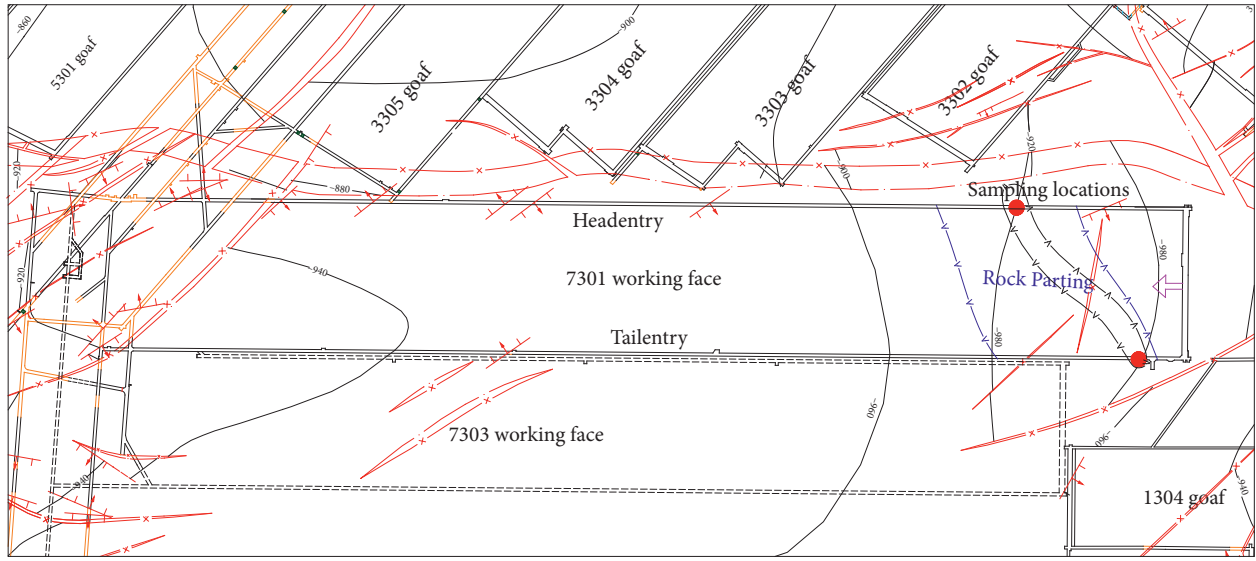


FIGURE 1: Plane sketch of the 7301 working face.

TABLE 1: Physical and mechanical properties of the rock parting, roof, and floor.

Material	Lithology	Thickness (m)	UCS (MPa)
Rock parting	Mudstone	0.7–1.6 (average = 1.1)	30–35
Immediate roof	Medium sandstone and mudstone	0–3.48 (average = 2.93)	35–40.5
Primary roof	Fine sandstone	7.7–12.9 (average = 9.61)	70.7–85.4
Immediate floor	Mudstone and siltstone	0–11.76 (average = 10.85)	28.6–44.2
Primary floor	Siltstone	10.3–11.9 (average = 11.03)	60.1–71.6

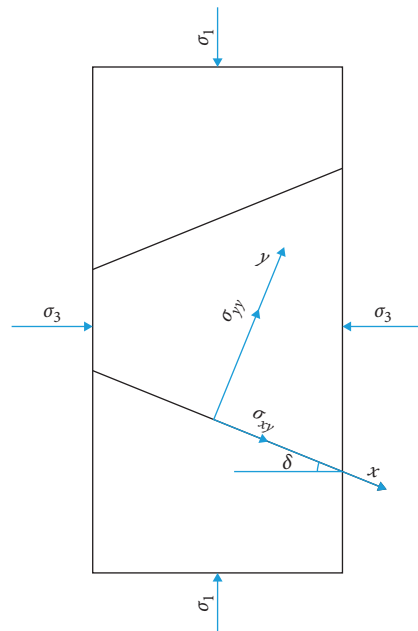


FIGURE 2: Mechanical model of CRCS.

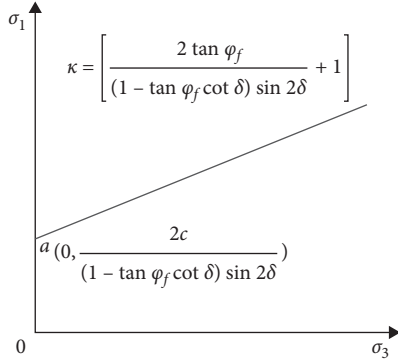


FIGURE 3: The relationship between σ_1 and σ_3 .

$$\delta_1 \geq \frac{2c}{(1 - \tan \varphi_f \cot \delta) \sin 2\delta} + \left(\frac{2 \tan \varphi_f}{(1 - \tan \varphi_f \cot \delta) \sin 2\delta} + 1 \right) \sigma_3. \quad (7)$$

From Figure 3, when the basic mechanical parameters of the interface (φ_f , δ , and c) are kept unchanged, the increase of σ_1 or the decrease of σ_3 can promote the slip of interface. To investigate the influencing effects of σ_1 and σ_3 on slip and instability process of CRCS, the UDEC numerical simulations were conducted.

3. Calibrations of Micromechanical Parameters of Coal and Rock Parting

The coal-rock and rock parting samples were cored from the headentry and tailentry of the 7301 working face. According to the standard of uniaxial compressive test of the International Society for Rock Mechanics (ISRM), the coal-rock and rock parting were processed to cylindrical samples with the diameter of 50 mm and the height of 100 mm. The size of numerical simulation model is consistent with that of the samples tested in laboratory. It was placed between two platens, the top platen moved down by displacement-control method with constant loading rate, whereas the bottom one was fixed. The vertical force was recorded by the monitoring line set in the bottom platen.

3.1. Effects of Block Size. For the UDEC models, an elastic and variable triangular unit assembly (block) was used to model the coal-rock and rock parting. The triangular units are bonded by contact, and the damage of coal and rock parting is described by shear or tensile failure of the contact between them. The contact obeys the Coulomb-slip model with residual strength. The elastic blocks do not generate damage, and the development of cracks occurs only at the contact between blocks. Thus, the block size determines the crack scale and the corresponding development characteristics. Figure 4 shows the crack development of the models with average block edge length of 6, 4, and 2 mm and a coal sample tested in laboratory.

In Figure 4(a), the cracks are mainly located in the upper-left corner and the middle-right side of the sample, which are characterized by external tensile failure and internal shear failure. From Figure 4(b), the cracks propagate along the middle line of the sample, characterized by middle shear failure and significant tensile failure along two lateral sides. From Figure 4(c), the internal cracks of the sample connect with the marginal fissures. The dominant tensile cracks on the left side manifest splitting failure (the fracture along the loading direction), and the dominant shear cracks on the right side show shear failure. Figure 4(d) shows the failure characteristics of coal sample under uniaxial compression in laboratory. The splitting failure generates on the left side and shear cracks form on the right side, which is basically consistent with crack development and failure characteristics shown in Figure 4(c). Therefore, the smaller block size can meet laboratory results. However, the operation time of the model will be significantly increased if the block size is too small. Thus, the block size should be reasonably chosen according to the criterion that it does not obviously affect failure mechanism of coal and rock mass.

3.2. Effects of Loading Rate. The loading rate has an important influence on the failure characteristics of numerical model [29]. The smaller the loading speed, the more stable the model damage. However, smaller loading rate will significantly increase the operation time of the model. Thus, it is necessary to select the appropriate loading rate. Figure 5 shows the axial stress versus vertical strain with four different loading rates of 0.02, 0.05, 0.08, and 0.15 m/s, respectively. It is important to point out that the unit of m/s is the default velocity format in UDEC software. The true loading rate can be interpreted by multiplying the platen velocity by mechanical timestep, which is about 6.215×10^{-8} s/step in these models, and thus the actual loading rate is $1.2-9.3 \times 10^{-6}$ mm/step.

From Figure 5, the similar stress-strain curves were produced by four different loading rates before peak strength, and the post-peak behaviour was obviously different. With the increase of loading rate, the unstable failure of the models becomes more significant. In order to reduce error and make the operation time acceptable, the loading rate of 0.05 m/s was chosen.

3.3. Calibration Process. The calibration adopted an elastic block model with an average side length of 2 mm. The contact obeys the Coulomb-slip model with residual strength. The micromechanical parameters of block and contact surface cannot be directly obtained through laboratory tests. The calibration is mainly based on the comparisons between simulation results and macromechanical parameters obtained in laboratory. Then, the micromechanical parameters are modified using the trial and error approach until the simulation results are in good agreement with the laboratory results.

3.4. Rationality Analysis of Micromechanical Parameters. The main variables include stress, strain, and joint failure modes. Calibration curves of coal and mudstone (rock

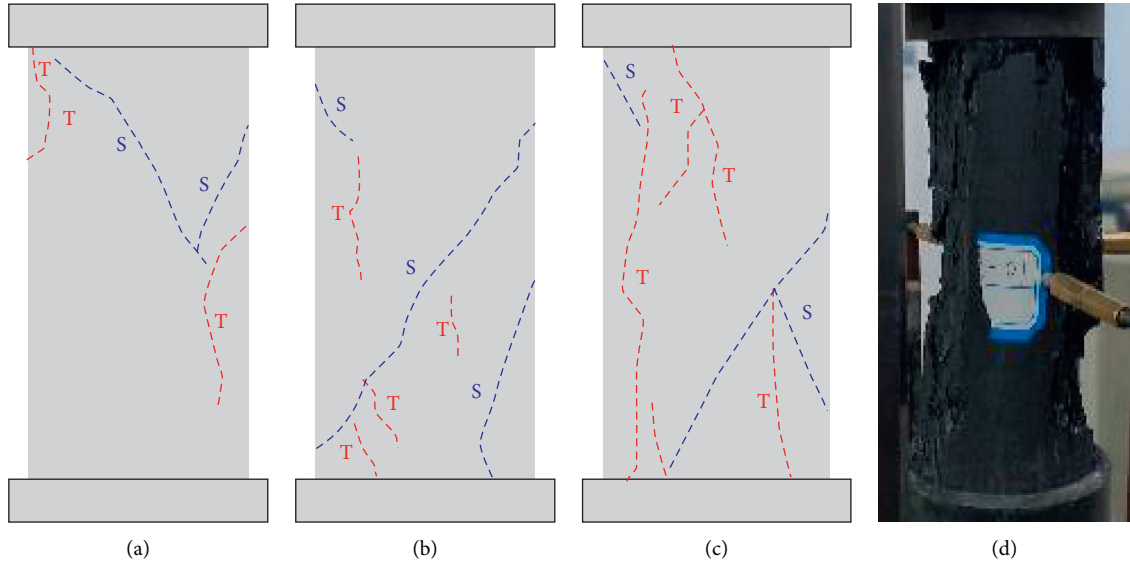


FIGURE 4: . Influencing effects of block size on crack development: (a) 6 mm, (b) 4 mm, (c) 2 mm, and (d) physical test.

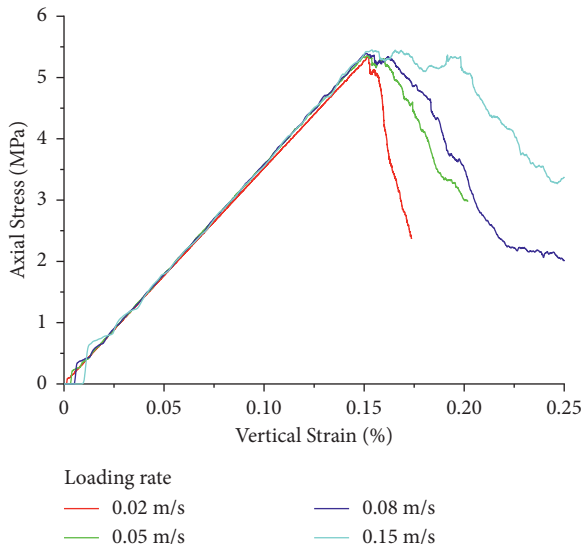


FIGURE 5: Axial stress versus vertical strain with different loading rates.

parting) subjected to uniaxial compression by tests in laboratory and numerical simulations are shown in Figure 6. The micromechanical parameters of coal and mudstone after calibrations are given in Table 2.

Crack initiation stress or threshold is defined by the onset of stable crack growth. The crack starts to appear systematically when stress is higher than the crack initiation stress [30, 31]. From Figure 6, the coal and mudstone samples produced initial crack with stress value equal to 50.33% and 59.75% of UCS, respectively, indicating tensile fracture. Thus, the stress value can be taken as initial threshold of sample damage. The crack damage stress is defined as the stress where a drastic increase of crack activity is observed [32–34]. The number of cracks in coal and mudstone samples developed rapidly after shear cracks

appeared. Therefore, the stress value of initial shear cracks can be used as the threshold of crack damage, which was 95.33% and 92.92% of UCS, respectively. Previous studies on the law of coal fracture development have been reported [35–37], and it was clarified that the thresholds for crack initiation and damage were 40% to 60% and 70% to 90% of UCS, respectively. The UCS and elastic modulus of coal and rock by tests in laboratory and numerical simulations are shown in Table 3. The errors of UCS were 1.36%, 1.77%, 2.13%, and 1.48% and that of elastic modulus were 3.95%, 4.37%, 10.10%, and 7.31%, respectively, indicating the good agreement between laboratory tests and simulations. Simultaneously, it was proved that the microparameters in Table 2 can better reflect the macromechanical properties of coal and rock parting, and the microparameters are feasible.

4. Slip and Instability Simulations of CRCS

4.1. Modelling. The numerical model of roadway excavation and mining of the 7301 working face is shown in Figure 7. The length and width of the model are 150 and 78 m, respectively, with the buried depth of 1000 m. The vertical stress is applied to the upper boundary of the model to simulate overburden, the horizontal displacement is constrained along the lateral boundaries, and the vertical and horizontal displacements are fixed at the bottom boundary. The UDEC-Trigon block was used to simulate the slip and instability process of the interface. The surrounding part of the model was divided into rectangular blocks which can better simulate the process of roof fall.

The Fish function “ZONK-FIS” in the UDEC was used to simulate stress release process by excavation. The simulation was divided into 10 stages, and 10% of the original stress was released at each stage until the stress was 0. The model was run in enough steps to reach the configured unbalanced force ($1e-5$) at each coefficient. The “cable,” “bolt,” and “structure” elements in the UDEC were adopted in roadway

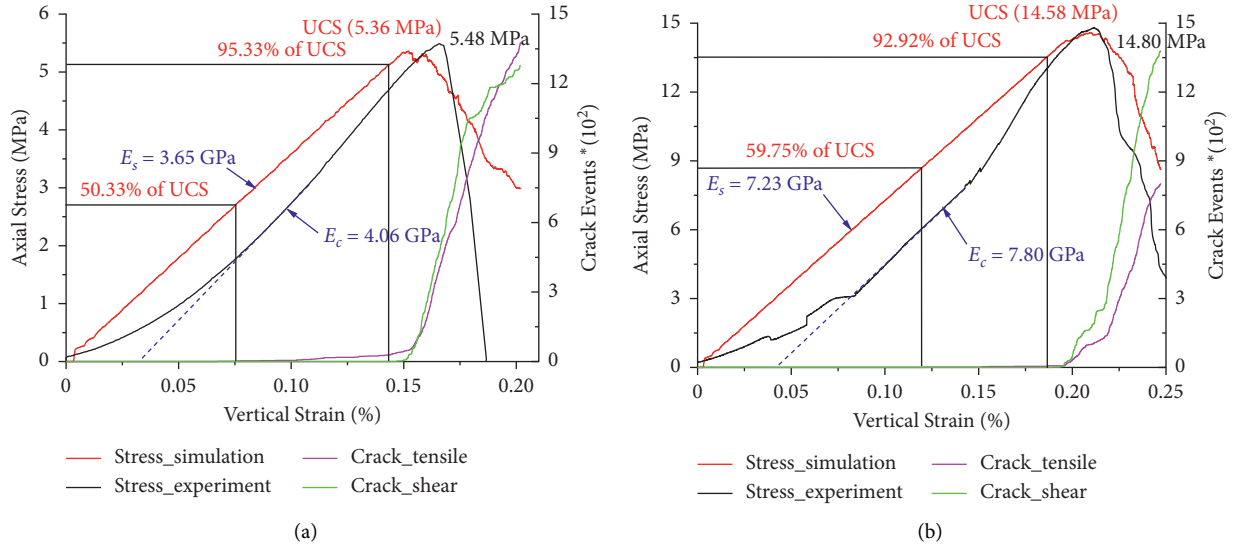


FIGURE 6: . Results of uniaxial compressive tests and numerical simulations of coal and mudstone: (a) coal and (b) mudstone.

TABLE 2: Joint parameters of the model.

Mineral	Block properties				Content properties					
	Density (GPa/m)	E (GPa/m)	k_n (GPa/m)	k_s (GPa/m)	Coh. (MPa)	Fri. ($^\circ$)	Ten. strength (MPa)	Res. coh. (MPa)	Res. fri. ($^\circ$)	Res. ten. strength (MPa)
Fine sandstone	2400	15.2	32426	12970.4	4.6	32	2.2	0	25	0
Siltstone	2600	9.62	21258	8503.2	3.3	30	1.8	0	26	0
Coal	1400	4.06	5876	2350.4	2.7	24	1.0	0	20	0
Mudstone	2400	7.80	14488	5795.2	6.4	30	3.4	0	24	0

TABLE 3: Comparisons of UCS and elastic modulus of coal and rock between experiments and simulations.

Mineral	UCS (MPa)			Error (%)	E (GPa)			Error (%)
	Experiment	Simulation			Experiment	Simulation		
Fine sandstone	78.62	77.55	1.36	15.2	14.6	3.95		
Siltstone	38.96	39.65	-1.77	9.62	9.20	4.37		
Coal	5.48	5.36	2.19	4.06	3.65	10.10		
Mudstone	14.80	14.58	1.48	7.80	7.23	7.31		

support during mining process. The rock bolts and cables were represented as a built-in “Cable” element, and the structure was represented as a built-in “Beam” element [38]. The parameters of the “Cable” and “Beam” elements are given in Table 4. The mining was divided into eight stages with each of 10 m. The mining of the next stage will be carried out until static balance of the previous stage.

4.2. Results and Analysis

4.2.1. Rock Parting Slip Triggered by Roadway Excavation.

(1) Fracture and slip of rock parting: a line-monitoring horizontal displacement was set with the interval of 0.5 m, and a total of 30 points were set for each line. The horizontal displacement value of each point is shown in Figure 8. The black vertical line in middle part represents the rock parting

sandwiched between top and bottom coal blocks. The difference of horizontal displacements of the monitoring points indicates the fracture level of rock parting, and the difference of the points on both sides of the interface indicates slip. The fluctuation of horizontal displacement indicates the fracture of blocks. For the line of the 118 m, the fluctuating displacement in the rock area indicates obviously shear failure. Meanwhile, the horizontal displacement of the rock parting is larger than that of coal blocks, which indicates that obvious shear fracture and slip along the interfaces generate in the rock parting. However, for the lines of 118.5, 119, and 119.5 m, there are obvious differences of horizontal displacement at the interfaces, while that of the rock parting are approximately equal, indicating only slip without obvious fracture. For the line of 120 m, the horizontal displacements of coal and rock parting along the interfaces are basically same, which is contrary to that of the lines of 118.5, 119, and

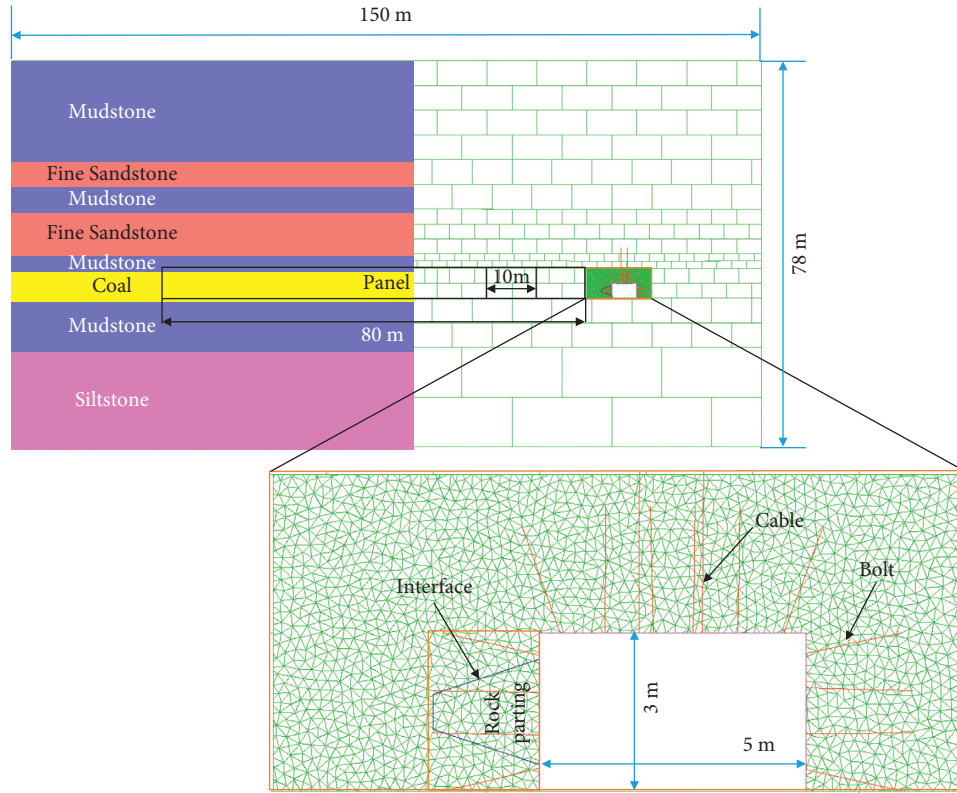


FIGURE 7: Numerical model of roadway excavation and mining activities.

TABLE 4: Support element properties in the model.

	Property	Value
Cable	Elastic modulus (GPa)	120
	Tensile yield strength (kN)	260
	Stiffness of the grout (N/m ²)	6.3e9
	Cohesive capacity of the grout (N/m)	6e6
Beam	Elastic modulus (GPa)	120
	Tensile yield strength (kN)	500
	Compressive yield strength (kN)	500
	Interface normal stiffness (GPa/m)	13.5
	Interface shear stiffness (GPa/m)	13.5

119.5 m. It is proved that the rock parting between the lines of 119.5 and 120 m generates reversed splitting failure. Thus, the failure of the rock parting is characterized by “shear fracture–slip-reversal splitting failure” from inside to outside, as shown in Figure 9.

(2) Crack evolution in CRCS: the process of crack initiation, propagation, and connection in CRCS after roadway excavation is shown in Figure 9. With the gradual release of the horizontal stress, cracks in coal and rock parting increase gradually. When the initial horizontal stress is reduced by 50%, the shear cracks first develop in the bottom coal block. When 60% is reduced, shear cracks begin to appear in the upper coal block and along the interface. Meanwhile, the rock parting begins to slip. When 70% is reduced, the side at bottom corner of the roadway generates slip and fracture. When 80% is released, shear cracks develop rapidly along the interface in vertical direction. Simultaneously, the rock

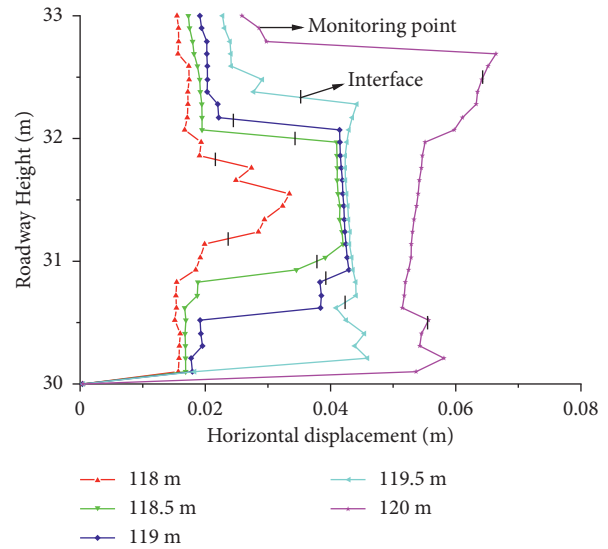


FIGURE 8: Horizontal displacement of vertical monitoring points in coal and rock parting.

parting of the lower interface also generates tensile failure in the process of slip and fracture of bottom coal. When 90% is reduced, the dominant shear cracks along the interfaces develop rapidly. When the horizontal stress is 0, the tensile cracks develop rapidly, and shear cracks connect, coalesce, and form macro cracks. The ratio of shear to tensile cracks is about 8.5:1. Therefore, it can be extrapolated that the fracture of the rock parting is dominantly characterized by

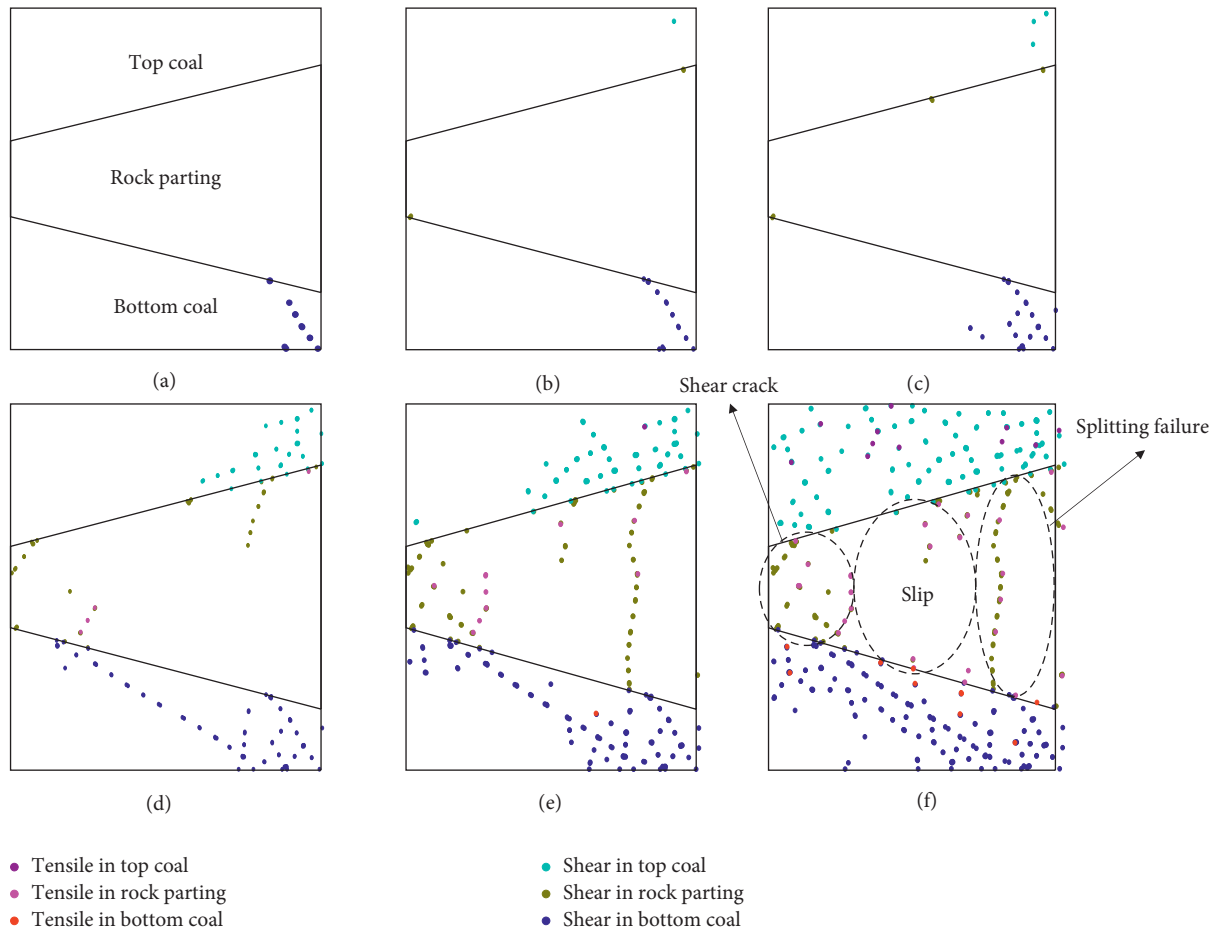


FIGURE 9: Crack evolution process in CRCS during horizontal stress release.

shear cracks while failure and instability of CRCS is mainly contributed to tensile cracks.

(3) Horizontal stress, shear stress, and shear displacement: the variations of horizontal stress, and shear stress and shear displacement of upper and lower interfaces by roadway excavation are shown in Figure 10.

From Figure 10, roadway excavation is accompanied with gradual release of horizontal stress, while shear stress is characterized by first increasing and then decreasing. When 40% of the initial horizontal stress is reduced, the interface begins to slip. Before slip, the shear stresses of upper and lower interfaces gradually increase with the decreasing horizontal stress. Meanwhile, the total energy of the CRCS is in process of release, while the energy in shear direction gradually accumulates. With the decrease of the horizontal stress, shear stress gradually increases to a peak stress of 5.29 MPa. After slip, shear stresses of two interfaces reduce gradually with the decrease of the horizontal stress, accompanied with the increase of slip velocity. When the horizontal stress is equal to 0, the slip of upper and lower interfaces reaches the maximum values of 0.067 and 0.058 m, respectively, with energy release of CRCS in shear direction. For each stress release stage, shear stresses of two interfaces obviously fluctuate, which is similar to the stick-slip effect. After stick-slip, shear stress gradually

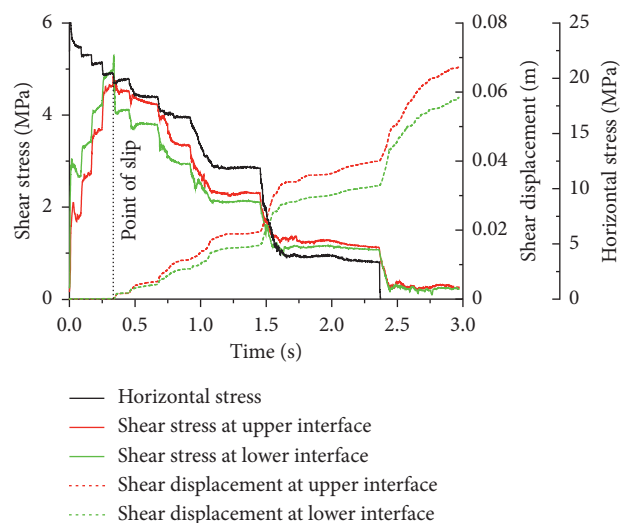


FIGURE 10: Horizontal stress, shear stress, and shear displacement of upper and lower interfaces.

approaches to a steady state, followed by stable slip. Therefore, it can be verified that the CRCS will produce obvious stick-slip phenomenon due to excavation, and then followed by stable slip.

(4) Damage rate and energy dissipation: to further explain the slip and failure of CRCS in the process of stress release due to excavation, the damage rate D is defined as follows:

$$D = \frac{S_D}{S_O} \times 100\%, \quad (8)$$

where S_D is the length of the damaged joint and S_O is the total length of the joint.

The damage rate and energy consumption by cracking in CRCS during excavation are shown in Figure 11.

From Figure 11, the damage rate of CRCS is characterized by stepped rise with the horizontal stress release. At initial stage of stress release, the CRCS remains stable without obvious cracking. When 40% of the initial stress is reduced, the slip occurs along the interfaces between coal and rock parting, and cracks begin to develop in the bottom coal. With the releasing of the stress, cracks gradually develop in the rock parting and top coal. When the stress is 0, the damage rate of each sublayer reaches the maximum and from bottom to top is 45.12%, 16.66%, and 44.67%, respectively. Smaller damage rate of the rock parting is due to the fact that its strength is higher than that of the coal. In addition, the total energy consumed by damage varies gradually with the stress release at each stage. Before 90% of the stress release, the total energy consumption rises gradually with the increase of stress release and decreases gradually after 90%. When stress release is completed, the increment of crack number is the largest, while the energy loss forming cracks is obviously reduced, indicating the rapid release of elastic energy in the CRCS and higher energy consumption by cracking. When the stress is completely released, both the elastic energy and energy consumption are gradually reduced.

In general, excavation is a process of transforming stress of surrounding coal-rock from three-dimensional state to plane state, accompanied with gradual release of elastic energy. With the release of stress and energy, the horizontal stress σ_3 around the roadway decreases gradually, and then shear stress along the interface between coal and rock parting increases, thus causing slip of the interface. With the stress release, the accumulated elastic energy is released rapidly, which intensifies crack development in the CRCS.

4.2.2. Rock Parting Slip Triggered by Mining Activity. (1) Roof caving: the starting date of mining activity of the 7301 working face is 4 June, 2019. Until July 12, the advancing distances of the tailentry and headentry were 87.4 and 88.7 m, respectively. The limit of designed mining speed is 4 m/d.

The first caving of the immediate roof occurred on 20 June, 2019, with the caving interval of 27 (tailentry) and 21.75 m (headentry). The first caving of the primary roof occurred on June 27, with the caving interval of 40.25 and 46 m at the tailentry and headentry, respectively. In addition, two periodic caving of primary roof were observed and recorded on July 5 and July 12. According to the pressuring and advancing distance, it is verified that the periodic caving

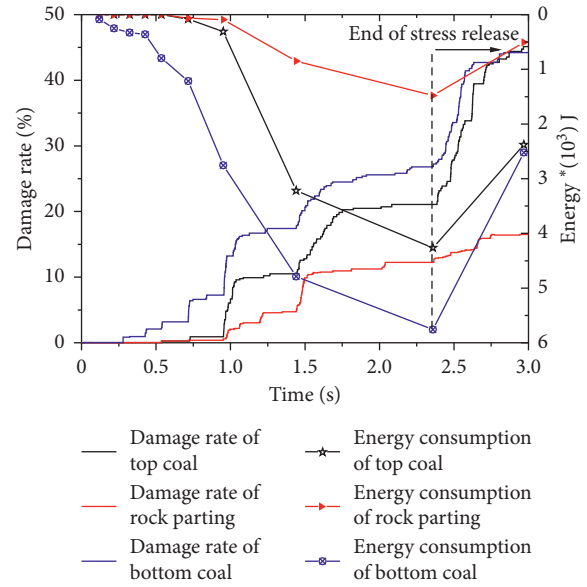


FIGURE 11: Damage rate and energy consumption by cracking in CRCS.

interval is about 21 m. Figure 12 shows the process of roof caving.

From Figure 12, the immediate roof began to fracture when the advancing distance reached 30 m, and then regularly fall with mining. When the advancing distance was 50 m, the primary roof began to fall, and the second caving occurred after continuous advancing distance of about 20 m, indicating that the periodic caving interval of primary roof was about 20 m. The aforementioned simulation results are basically consistent with real roof caving process monitored in the 7301 working face, indicating that the parameters used in the simulations are reasonable.

(2) Fracturing and slipping process of CRCS: the process of rock parting slip and roadway failure subjected to the front abutment pressure by mining activity was reproduced, as shown in Figure 13.

From Figure 13, the front abutment pressure of the 7301 working face gradually acts on the CRCS in the process of advancing and cracks around the roadway initiate and develop gradually, resulting in slip at the interface. When the advancing distance of the working face reaches 30 and 40 m, cracks cluster in the lower coal, and the number of cracks gradually decreases from the lower coal to the upper coal. The slippages between the upper coal and rock parting are 9.5 and 9.7 mm, respectively. When 50 m of the advancing distance is reached, cracks around the rock parting gradually converge and connect, and the crack density near the interfaces is obviously higher than that in the coal and rock parting. Meanwhile, the horizontal slippage increases to 14.9 mm, indicating obvious slip of the CRCS. When the advancing distance reaches 60 m, cracks around the roadway expand rapidly, and the horizontal slippage between the rock parting and coal further increases to 30.6 mm. When the advancing distance is 70 m, the top coal side produces obvious rib spalling, accompanied with the horizontal slippage of 72.1 mm. When the advancing distance is 80 m, cracks around the roadway coalesce rapidly, resulting in

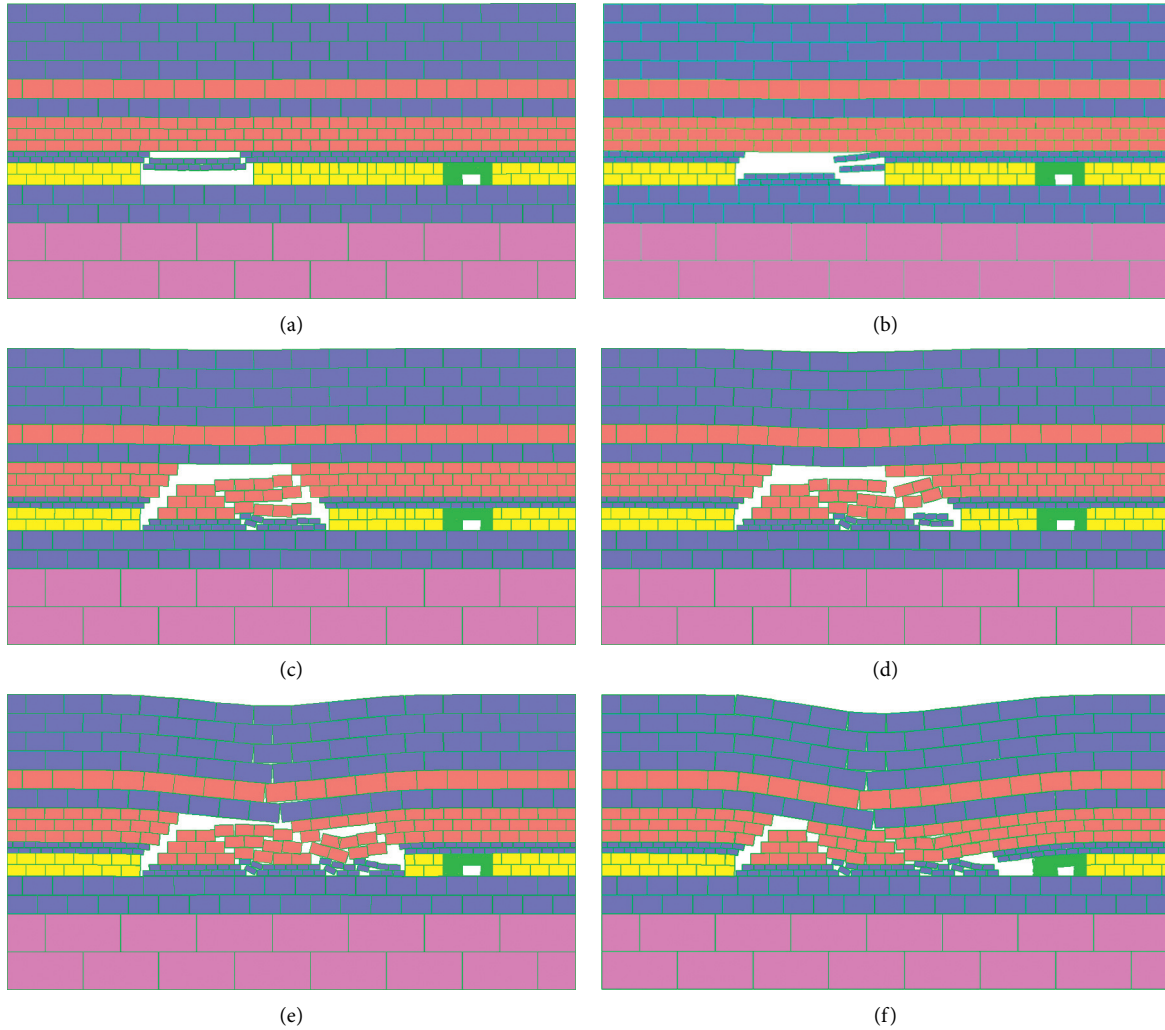


FIGURE 12: . Simulations of the roof caving process: (a) 30 m, (b) 40 m, (c) 50 m, (d) 60 m, (e) 70 m, and (f) 80 m.

obvious deformation and failure. The horizontal slippage reaches 200 mm. Therefore, it can be verified that the increase of vertical stress can promote the slip and instability of CRCS.

(3) Vertical stress, shear stress, and shear displacement: the variations of vertical stress, shear stress, and shear displacement of upper and lower interfaces along with mining of the working face are shown in Figure 14.

From Figure 14, the vertical stress rises obviously when the advancing distance is 50 m. Meanwhile, the front abutment pressure begins to act on the CRCS. Subsequently, each mining stage causes the increase of the vertical stress, accompanied by gradual increase of shear stress and shear displacement of upper and lower interfaces. In addition, the variation of the vertical stress is almost consistent with that of the shear stress. When the advancing is 80 m, both the vertical stress and shear stress reach the peak. Wang et al. pointed out that mining will cause the increase of front abutment pressure of a working face and thus shear stress along the interface will correspondingly rise, thereby triggering slip and instability of CRCS [39]. In the process of rock parking slip, the shear stress fluctuates and gradually

reaches equilibrium. Therefore, the vertical stress concentration in a coal seam containing rock parking will inevitably induce the additional shear stress along interfaces. Once the shear stress reaches or exceeds the threshold of slip, slip and instability will be inevitably induced, accompanied by transforming from stick-slip to steady-slip.

4.2.3. Case Verification. (1) Source clustering effect in the rock parting zone: the three-dimensional monitoring pattern of the seismological observation system (SOS) used a total of 16 geophones installed in underground roadways in the ZCM, and more than four geophones were arranged around the 7301 working face, which can locate the seismic sources with acceptable accuracy. Figure 15 shows the plane distribution of seismic sources in the 7301 working face during initial mining.

From Figure 15(a), the sources are obviously clustered in four zones, labelled as A, B, C, and D, respectively. The source ($E > 10^3$) concentrations of zones A and B were generated by slip and fracture of the interfaces accommodated between the rock parting layer and #3 coal, indicating

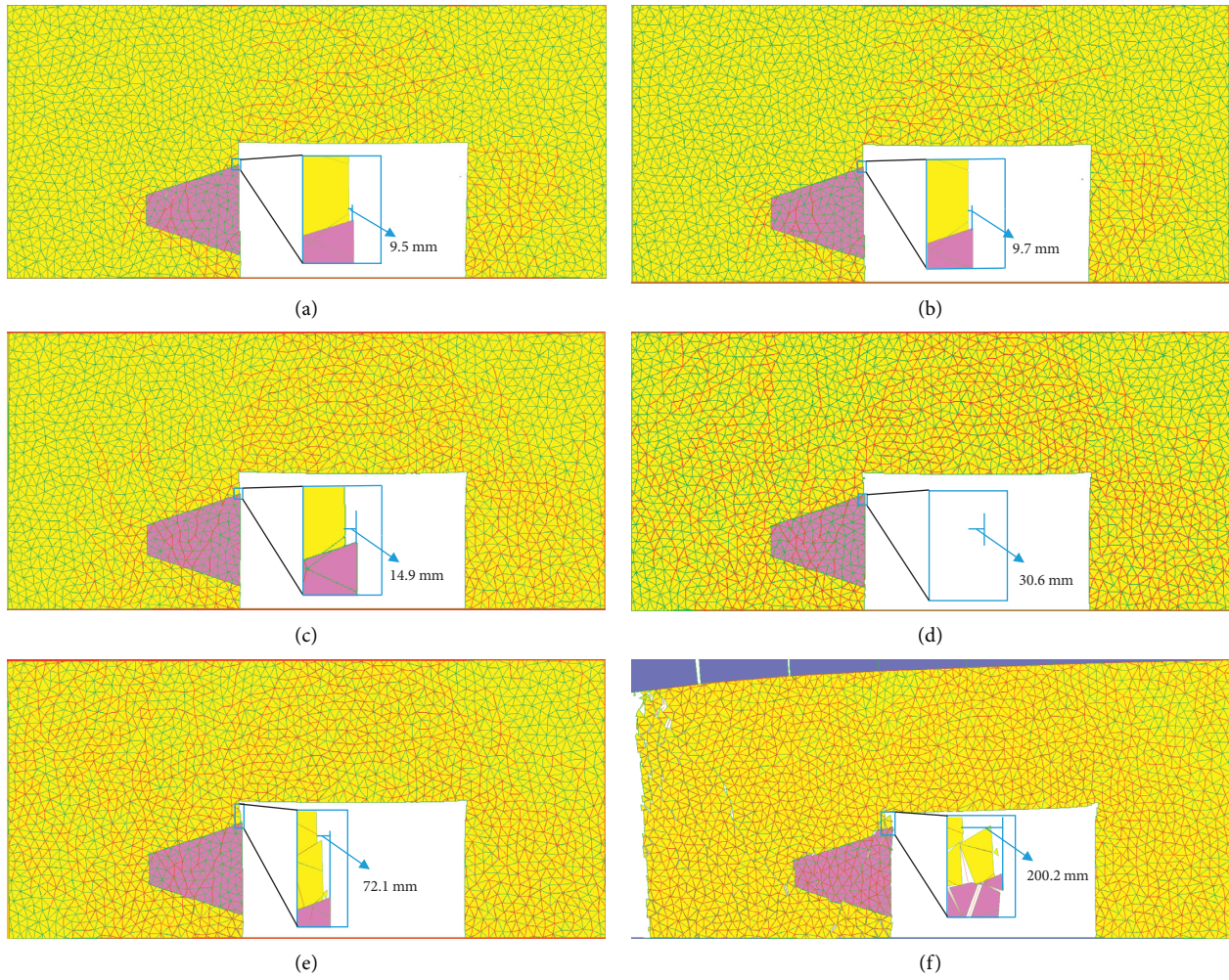


FIGURE 13: . Slip and failure process of CRCS: (a) 30 m, (b) 40 m, (c) 50 m, (d) 60 m, (e) 70 m, and (f) 80 m.

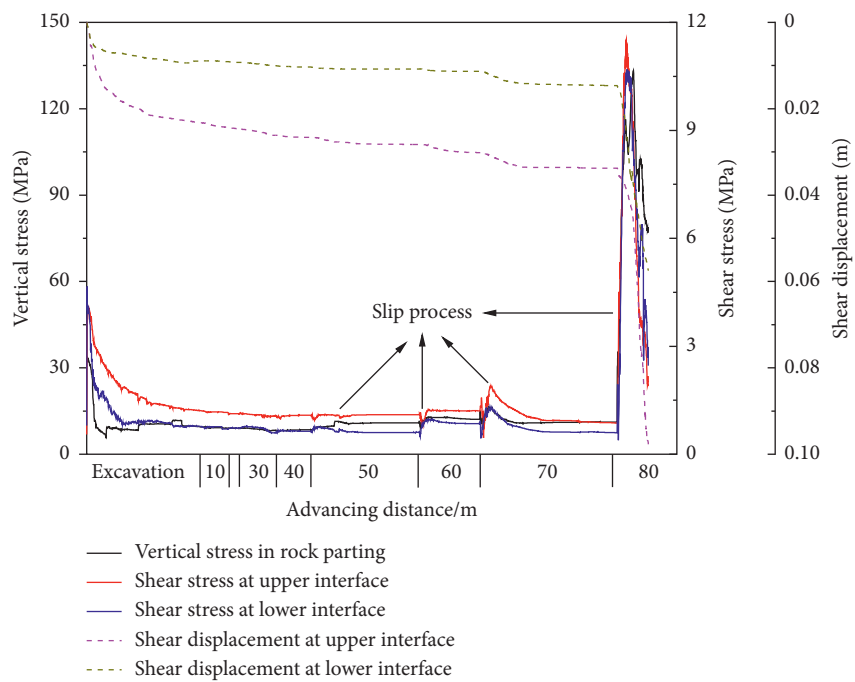


FIGURE 14: Vertical stress, shear stress, and shear displacement of upper and lower interfaces.

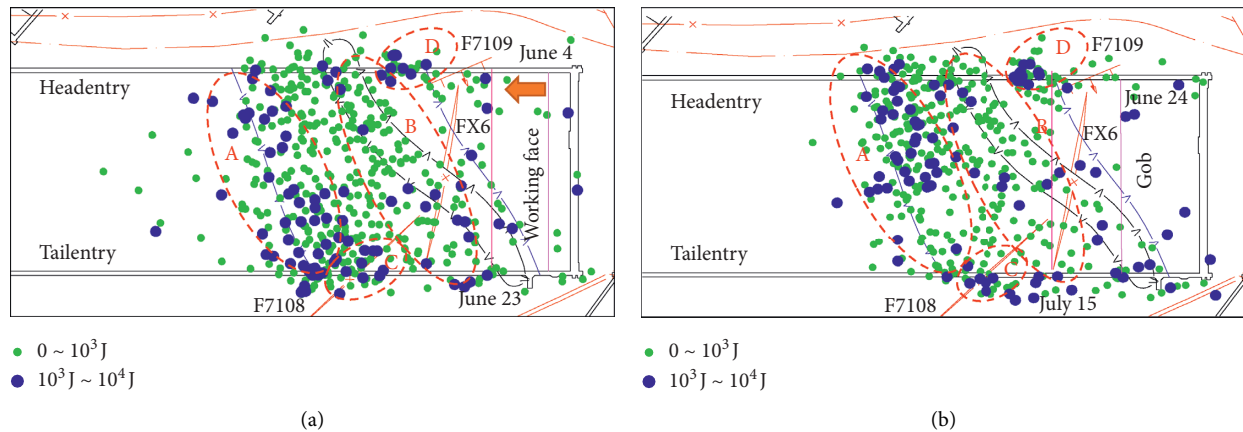


FIGURE 15: . Plane distributions of seismic sources in the rock parting area of the 7301 working face: (a) June 4–23 and (b) June 24–July 15.

that the vertical abutment pressure formed by mining caused obvious slip and fracture when advancing near the rock parting zone. The source ($E > 10^3$ J) concentrations of zones C and D were closely associated with the F7108 and F7109 fault activation with small throw induced by mining disturbance, whereas the sources did not obviously cluster around the FX6 fault. Based on Figure 15(b), the feature of the sources distribution did not obviously change along with mining of the working face, clustering in four zones, labelled as A, B, C, and D, respectively. In addition, some sources ($E > 10^3$ J) were located in gob, associated with the overlying roof strata fracture. Interestingly, the concentration zones of the sources were strictly consistent with the intruded zones of the rock partings in the 7301 working face, indicating that the interfaces between the #3 coal and rock partings generated slip and fracture during mining near the bifurcation zone.

(2) Passive inversion of the P-wave in the rock parting zone: the inversion of P-wave velocity in the rock parting based on the seismic events recorded from June 4 to July 15, 2019, is shown in Figure 16.

From Figure 16, the high P-wave velocity is significantly located in the rock parting zone, demonstrating static high stress concentration based on the relationship between P-wave velocity and the imposed stress of coal and rock [40, 41]. The stress concentration in the zone was caused by bifurcation of the #3 coal generated by the rock parting layer, whereas the fault F7109 and FX6 did not cause static stress concentration, which may be associated with the fracturing of coal and rock. Therefore, the high stress was associated with the discontinuities between the #3 coal and rock parting. The discontinuities subjected to dynamic stress disturbance along with the advancing to the rock parting zone generated slip and fracture, and therefore a large number of sources inevitably clustered in the zone, indicating high rockburst danger.

(3) Active inversion of rockburst danger index in the rock parting zone: active P-wave tomography was performed for evaluating rockburst danger in the rock parting zone before mining of the 7301 working face. The detection range was around 404 m ahead of the open cutting. A total of 58

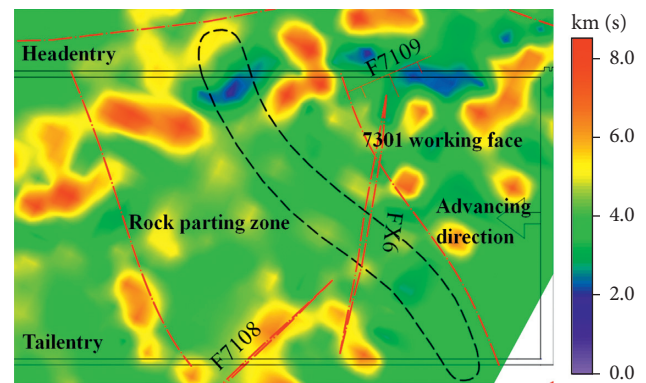


FIGURE 16: . Cloud chart of P-wave velocity distribution in the rock parting zone.

blasting sources were implemented in the headentry, and 22-channel receiver was set in the tailentry. The diameter of the blast hole was 42 mm, the depth was 2 m, and the spacing was 7 m. The spacing of the receiving substation was 18 m, and the #1 blast hole and first substation was arranged in the headentry and tailentry 5 m ahead of the open cutting, respectively. The distribution of rockburst danger index φ calculated by P-wave velocity is shown in Figure 17.

The rockburst danger index in the rock parting zone is higher associated with high static stress. With approaching to the rock parting zone, the dynamic stress disturbance is more and more significant. When the front abutment pressure triggering fracture and slip of the rock parting increases, the corresponding rockburst danger index rises. In summary, the inversions of P-wave velocity and rockburst danger index are consistent with the simulation results.

In conclusion, the stress unloading during excavation can enhance the impact risk of coal seam with rock parting. The decrease of horizontal stress and the increase of vertical stress can accelerate the slipping instability of coal and rock parting along the interface surface. This is also the main reason for frequent impact disaster in the area of excavating coal seam with rock parting. Therefore, in the process of excavation, the unloading speed of horizontal stress and the

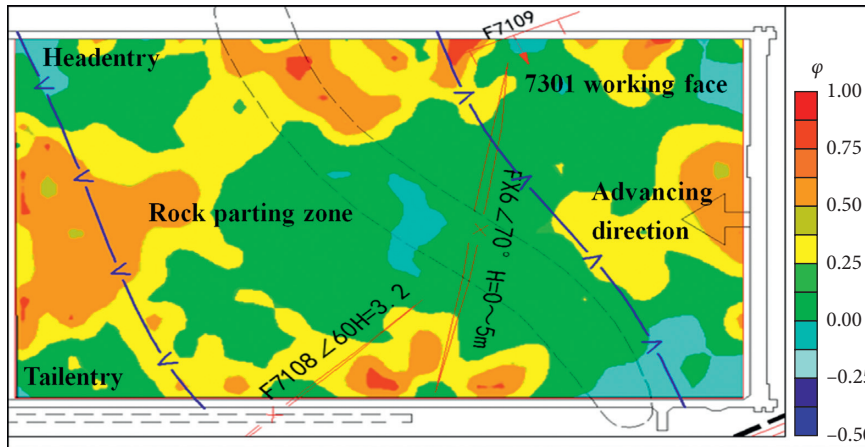


FIGURE 17: Cloud chart of rockburst danger index ϕ in the rock parting zone. Notes: the index ϕ denotes the rockburst danger level (safe: 0–0.25; weak: 0.25–0.5; medium: 0.5–0.75; strong: 0.75–0.1).

rising speed of vertical stress should be reduced as much as possible to make the process of stress redistribution more stable (for example, timely support, increasing support strength, and early grouting reinforcement), which will greatly reduce the possibility of impact disaster accidents.

5. Conclusion

- (1) Horizontal stress release caused by excavation will easily trigger the slip and instability of CRCS, and the damage of rock parting is partitioned into three parts: shear failure zone, slipping zone, and splitting failure zone from inside to outside. The ratio of shear to tensile cracks is about 8.5:1. The fracture of the rock parting is dominantly characterized by shear cracks while tensile crack is the main factor causing failure and instability of CRCS. The CRCS slip first shows obvious stick-slip and then followed by stable slip.
- (2) The vertical stress concentration by mining activity in a coal seam containing rock parking will induce the additional shear stress along the interfaces. Once the shear stress reaches or exceeds the threshold of slip, slip and instability will be inevitably induced, accompanied by transforming from stick-slip to steady-slip.
- (3) Both the horizontal stress release caused by excavation and vertical stress concentration caused by mining increase along the interfaces. Thus, the excavation and mining of a coal seam containing a rock parking layer will easily induce slip and instability of CRCS due to shear stress increase along the interfaces.
- (4) The interfaces subjected to mining disturbance along with advancing to the rock parting zone generate slip and fracture, and thus a large number of seismic sources significantly cluster in the zone, accompanied with high P-wave velocity and high rockburst danger level due to stress concentration by passive

and active inversions. The inversions are consistent with the simulation results.

Data Availability

The data used in this manuscript are available from the authors.

Conflicts of Interest

The authors declare that there are no conflicts of interest.

Acknowledgments

The authors gratefully wish to acknowledge the Natural Science Foundation of Zhejiang Province (Grant no. LQ20E040002) and the Independent Research Project of State Key Laboratory of Coal Resources and Safe Mining, CUMT (Grant no. SKLCRSM19X005).

References

- [1] C. Bandopadhyay, P. R. Sheorey, B. Singh, and A. K. Ghose, "Stability of parting rock between level contiguous coal pillar workings," *International Journal of Rock Mechanics and Mining Science & Geomechanics Abstracts*, vol. 25, no. 5, pp. 307–320, 1988.
- [2] Z. Q. Wang, P. F. Wang, Q. Y. Zhong, and J. Zhou, "Treatment and utilization of dirt band between contiguous coal seams," *J Min Safety Eng*, vol. 35, pp. 960–968, 2016.
- [3] D. M. Guo, J. P. Zuo, Y. Zhang, and R. S. Yang, "Research on strength and failure mechanism of deep coal-rock combination bodies of different inclined angles," *Rock and Soil Mechanics*, vol. 32, pp. 1332–1339, 2011.
- [4] T. Wang, Y. Jiang, S. Zhan, and C. Wang, "Frictional sliding tests on combined coal-rock samples," *Journal of Rock Mechanics and Geotechnical Engineering*, vol. 6, no. 3, pp. 280–286, 2014.
- [5] T.-B. Zhao, W.-Y. Guo, C.-P. Lu, and G.-M. Zhao, "Failure characteristics of combined coal-rock with different interfacial angles," *Geomechanics and Engineering*, vol. 11, no. 3, pp. 345–359, 2016.

- [6] C.-P. Lu, G.-J. Liu, H.-Y. Wang, and J.-H. Xue, "Numerical investigation of rockburst effect of shock wave on underground roadway," *Shock and Vibration*, vol. 2015, pp. 1–10, 2015.
- [7] X. Si and F. Gong, "Strength-weakening effect and shear-tension failure mode transformation mechanism of rockburst for fine-grained granite under triaxial unloading compression," *International Journal of Rock Mechanics and Mining Sciences*, vol. 131, Article ID 104347, 2020.
- [8] Y. Liu, C.-P. Lu, H. Zhang, and H.-Y. Wang, "Numerical investigation of slip and fracture instability mechanism of coal-rock parting-coal structure (CRCS)," *Journal of Structural Geology*, vol. 118, pp. 265–278, 2019.
- [9] I. M. Petukhov and A. M. Linkov, "The theory of post-failure deformations and the problem of stability in rock mechanics," *International Journal of Rock Mechanics and Mining Science & Geomechanics Abstracts*, vol. 16, no. 2, pp. 57–76, 1979.
- [10] L. D. Suits, T. C. Sheahan, J. P. Seidel, and C. M. Harberfield, "Laboratory testing of concrete-rock joints in constant normal stiffness direct shear," *Geotechnical Testing Journal*, vol. 25, pp. 391–404, 2002.
- [11] B. Huang and J. Liu, "The effect of loading rate on the behavior of samples composed of coal and rock," *International Journal of Rock Mechanics and Mining Sciences*, vol. 61, pp. 23–30, 2013.
- [12] Z. Zhao, W. Wang, L. Wang, and C. Dai, "Compression-shear strength criterion of coal-rock combination model considering interface effect," *Tunnelling and Underground Space Technology*, vol. 47, pp. 193–199, 2015.
- [13] X. S. Liu, Y. L. Tan, J. G. Ning, Y. W. Lu, and Q. H. Gu, "Mechanical properties and damage constitutive model of coal in coal-rock combined body," *International Journal of Rock Mechanics and Mining Sciences*, vol. 110, pp. 140–150, 2018.
- [14] B. Ladanyi and G. Archambault, "Simulation of the shear behavior of a jointed rock mass," in *Proceedings of the 11th US Symposium on Rock Mechanics*, pp. 105–125, New York, NY, USA, June 1969.
- [15] H. Lippmann, "Mechanics of "bumps" in coal mines: a discussion of violent deformations in the sides of roadways in coal seams," *Applied Mechanics Reviews*, vol. 40, no. 8, pp. 1033–1043, 1987.
- [16] Y.-l. Tan, W.-y. Guo, Q.-h. Gu et al., "Research on the rockburst tendency and AE characteristics of inhomogeneous coal-rock combination bodies," *Shock and Vibration*, vol. 2016, no. 2, 11 pages, Article ID 9271434, 2016.
- [17] W. Li, J. Bai, J. Cheng, S. Peng, and H. Liu, "Determination of coal-rock interface strength by laboratory direct shear tests under constant normal load," *International Journal of Rock Mechanics and Mining Sciences*, vol. 77, pp. 60–67, 2015.
- [18] Z.-h. Zhao, W.-m. Wang, C.-q. Dai, and J.-x. Yan, "Failure characteristics of three-body model composed of rock and coal with different strength and stiffness," *Transactions of Nonferrous Metals Society of China*, vol. 24, no. 5, pp. 1538–1546, 2014.
- [19] S. Mehrishal, M. Sharifzadeh, K. Shahriar, and J.-J. Song, "An experimental study on normal stress and shear rate dependency of basic friction coefficient in dry and wet limestone joints," *Rock Mechanics and Rock Engineering*, vol. 49, no. 12, pp. 4607–4629, 2016.
- [20] A. M. Alzo'ubi, *The effect of tensile strength on the stability of rock slopes*, Ph.D. thesis, University of Alberta, Edmonton, Canada, 2009.
- [21] A. M. Alzo'ubi, "Modeling of rocks under direct shear loading by using discrete element method," *Journal of Engineering Applied Sciences*, vol. 4, pp. 5–20, 2012.
- [22] F. Gao, D. Stead, and H. Kang, "Simulation of roof shear failure in coal mine roadways using an innovative UDEC Trigon approach," *Computers and Geotechnics*, vol. 61, pp. 33–41, 2014.
- [23] F. Q. Gao and D. Stead, "The application of a modified Voronoi logic to brittle fracture modelling at the laboratory and field scale," *International Journal of Rock Mechanics and Mining Sciences*, vol. 68, pp. 1–14, 2014.
- [24] Y. Zheng, C. Chen, T. Liu, H. Zhang, K. Xia, and F. Liu, "Study on the mechanisms of flexural toppling failure in anti-inclined rock slopes using numerical and limit equilibrium models," *Engineering Geology*, vol. 237, pp. 116–128, 2018.
- [25] C.-P. Lu, G.-J. Liu, Y. Liu, and H. Zhang, "Mechanisms of rockburst triggered by slip and fracture of coal-parting-coal structure discontinuities," *Rock Mechanics and Rock Engineering*, vol. 52, no. 9, pp. 3279–3292, 2019.
- [26] W. T. Li, S. C. Li, C. Xuan, W. Qingfei, X. Wang, and W. Shao, "Mechanism and control of failure of rock roadway support in highly stressed soft rock," *Chinese Journal of Rock Mechanics and Engineering*, vol. 34, pp. 1836–1848, 2015.
- [27] F. Gao, D. Stead, and J. Coggan, "Evaluation of coal longwall caving characteristics using an innovative UDEC Trigon approach," *Computers and Geotechnics*, vol. 55, pp. 448–460, 2014.
- [28] D. L. Tien, J. Oh, H. Bruce, C. Zhang, and R. Mitra, "A discontinuum modelling approach for investigation of longwall top coal caving mechanisms," *International Journal of Rock Mechanics and Mining Sciences*, vol. 106, pp. 84–95, 2018.
- [29] Q.-S. Bai, S.-H. Tu, and C. Zhang, "DEM investigation of the fracture mechanism of rock disc containing hole(s) and its influence on tensile strength," *Theoretical and Applied Fracture Mechanics*, vol. 86, pp. 197–216, 2016.
- [30] W. Q. Ma and T. X. Wang, "Compression failure characteristics and crack propagation of brittle rock under various confining pressures," *Chinese Journal of Rock Mechanics and Engineering*, vol. 37, pp. 898–908, 2018.
- [31] N. Cho, C. D. Martin, and D. C. Segol, "A clumped particle model for rock," *International Journal of Rock Mechanics and Mining Sciences*, vol. 44, no. 7, pp. 997–1010, 2007.
- [32] J. S. Yoon, A. Zang, and O. Stephansson, "Simulating fracture and friction of Aue granite under confined asymmetric compressive test using clumped particle model," *International Journal of Rock Mechanics and Mining Sciences*, vol. 49, pp. 68–83, 2012.
- [33] M. Cai, P. K. Kaiser, Y. Tasaka, T. Maejima, H. Morioka, and M. Minami, "Generalized crack initiation and crack damage stress thresholds of brittle rock masses near underground excavations," *International Journal of Rock Mechanics and Mining Sciences*, vol. 41, no. 5, pp. 833–847, 2004.
- [34] T. Kazerani and J. Zhao, "Micromechanical parameters in bonded particle method for modelling of brittle material failure," *International Journal for Numerical and Analytical Methods in Geomechanics*, vol. 34, no. 18, pp. 1877–1895, 2010.
- [35] E. Hoek and C. D. Martin, "Fracture initiation and propagation in intact rock - a review," *Journal of Rock Mechanics and Geotechnical Engineering*, vol. 6, no. 4, pp. 287–300, 2014.
- [36] L. Xue, S. Qin, Q. Sun, Y. Wang, L. M. Lee, and W. Li, "A study on crack damage stress thresholds of different rock types based on uniaxial compression tests," *Rock Mechanics and Rock Engineering*, vol. 47, no. 4, pp. 1183–1195, 2014.

- [37] X. Li, M. Ju, Q. Yao, J. Zhou, and Z. Chong, "Numerical investigation of the effect of the location of critical rock block fracture on crack evolution in a gob-side filling wall," *Rock Mechanics and Rock Engineering*, vol. 49, no. 3, pp. 1041–1058, 2016.
- [38] F. Gao, D. Stead, H. Kang, and Y. Wu, "Discrete element modelling of deformation and damage of a roadway driven along an unstable goaf - a case study," *International Journal of Coal Geology*, vol. 127, pp. 100–110, 2014.
- [39] J.-c. Wang, F.-x. Jiang, X.-j. Meng, X.-y. Wang, S.-t. Zhu, and Y. Feng, "Mechanism of rock burst occurrence in specially thick coal seam with rock parting," *Rock Mechanics and Rock Engineering*, vol. 49, no. 5, pp. 1953–1965, 2016.
- [40] C.-P. Lu, G.-J. Liu, N. Zhang, T.-B. Zhao, and Y. Liu, "Inversion of stress field evolution consisting of static and dynamic stresses by microseismic velocity tomography," *International Journal of Rock Mechanics and Mining Sciences*, vol. 87, pp. 8–22, 2016.
- [41] G. J. Liu, Z. L. Mu, J. Atif, S. Gong, J. Yang, and J. Cao, "Investigation into mechanism of floor dynamic rupture by evolution characteristics of stress and mine tremors: a case study in guojiahe coal mine, China," *Shock and Vibration*, vol. 2018, Article ID 3279036, 13 pages, 2018.